

## **Attachment**

**Hydrothermal synthesis, characterization, and magnetic properties of cobalt chromite nanoparticles**

# Hydrothermal synthesis, characterization, and magnetic properties of cobalt chromite nanoparticles

D. Zákutná · A. Repko · I. Matulková ·  
D. Nižňanský · A. Ardu · C. Cannas ·  
A. Mantlíková · J. Vejpravová

Received: 24 August 2013 / Accepted: 6 January 2014  
© Springer Science+Business Media Dordrecht 2014

**Abstract** The  $\text{CoCr}_2\text{O}_4$  nanoparticles were prepared by hydrothermal treatment of chromium and cobalt oleates in a mixture of solvents (water and ethanol or pentanol) at various temperatures. The samples were further annealed at the temperatures from 300 to 500 °C. The obtained nanoparticles were characterized using powder X-ray diffraction (PXRD), transmission electron microscopy (TEM), high-resolution TEM, scanning electron microscopy, thermogravimetric analysis, Raman and infrared spectroscopy, and magnetic measurements. The particle size, ranging from 4.4 to 11.5 nm, was determined from the TEM and PXRD methods. The tendency of particles to form the aggregates with the increasing annealing

temperature has been observed. The magnetic measurements revealed that the typical features of the  $\text{CoCr}_2\text{O}_4$  long-range magnetic order are suppressed in the nanoparticles.

**Keywords** Cobalt chromite · Hydrothermal method · Nanoparticles · Size effect · Multiferroic materials

## Introduction

Up to date, the studies of magnetic nanomaterials were focused mostly on spinel ferrites due to their straightforward application potential in biomedicine, data storage, electronics, etc. However, there are only few works concerning isostructural chromite as nanoparticles (NPs) or thin films. The  $\text{MCr}_2\text{O}_4$  (where M is metal) compounds form a normal spinel structure, where the  $\text{M}^{2+}$  and  $\text{Cr}^{3+}$  are located in the tetrahedral ( $T_d$ ) and octahedral ( $O_h$ ) sites, respectively. They are known as multiferroic materials with complex magnetic phase diagrams and magnetic structure, where the ferroelectric order occurs in spite of nonzero spontaneous magnetization in the conical spin configuration (Lyons et al. 1962; Hastings and Corliss 1962; Menyuk et al. 1964; Shirane et al. 1964; Tomiyasu et al. 2004; Chang et al. 2009; Kim et al. 2009).

Among the spinel chromites, the  $\text{CoCr}_2\text{O}_4$  is the first example of a multiferroic compound with both the spontaneous magnetization and polarization of spin

---

D. Zákutná · A. Repko · I. Matulková · D. Nižňanský  
Department of Inorganic Chemistry, Faculty of Science,  
Charles University in Prague, Hlavova 2030,  
128 43 Prague 2, Czech Republic

D. Zákutná (✉) · A. Mantlíková · J. Vejpravová  
Institute of Physics of the ASCR, v.v.i, Department of  
Magnetic Nanosystems, Na Slovance 2, 182 21 Prague 8,  
Czech Republic  
e-mail: dominika.zakutna@gmail.com

D. Nižňanský  
Institute of Inorganic Chemistry, ASCR, 250 68 Řež near  
Prague, Czech Republic

A. Ardu · C. Cannas  
Università di Cagliari, Dipartimento di Scienze Chimiche,  
Complesso, Universitario di Monserrato,  
09042 Monserrato, CA, Italy

origin (Yamasaki et al. 2006), where the strong clamping between the ferromagnetic and ferroelectric domains, leading to the magnetic reversal of the ferroelectric polarization, has been observed. Concerning the magnetic order, the compound undergoes a ferromagnetic transition at  $T_C = 93$  K, and with the further lowering of temperature, the additional transition to the conical spin state occurs at 26 K. The so-called lock-in transition,  $T_{\text{lock-in}}$ , takes place around 15 K with minimal change of the propagation vector (Funahashi et al. 1987; Chang et al. 2009). Considering the size effects in chromites, a comprehensive work reports on  $\text{MnCr}_2\text{O}_4$  NPs prepared by high-energy ball milling, which points to unusual Bloch exponent value 3.35, which decreases and approaches a typical value of 1.5, as expected for a common ferromagnet, with decreasing particle size (Bhowmik 2006). Recently, several works also report on the  $\text{CoCr}_2\text{O}_4$  NPs obtained using various methods.

One of the first preparations of cobalt chromite NPs was carried out by Dutta et al. (2009). They reported the synthesis of nanocrystalline  $\text{CoCr}_2\text{O}_4$  by a fast sonochemical route, which was based on acoustic cavitations in a liquid. The final particle size was about 30–40 nm, and the magnetic properties were only slightly influenced in comparison to the bulk material. Rath and Mohanty (2010; Rath et al. 2011) prepared the  $\text{CoCr}_2\text{O}_4$  NPs of a mean size about 8 nm using a simple coprecipitation method and observed an unusual transition from paramagnetic to superparamagnetic (SPM) state. Edrissi and Keshavarz (2012) improved the preparation method using organic precursors:  $\text{Cr}^{3+}$  and  $\text{Co}^{2+}$  chelates of 2-mercaptopyridin *N*-oxide for the preparation of the cobalt chromite NPs. Durrani et al. (2012) prepared the cobalt chromite NPs by hydrothermal synthesis at higher values of pH (>10), and this procedure led to rather large particles (>100 nm).

So far, no work on preparation and physical properties of monodisperse cobalt chromite NPs with size below 20 nm has been reported, and, therefore, a study of magnetic and ferroelectric properties down to very low scales has not been possible yet. In order to reach the critical size range, we focused on preparation of the  $\text{CoCr}_2\text{O}_4$  NPs using hydrothermal method, successfully applied in the case of  $\text{CoFe}_2\text{O}_4$  NPs (Repko et al. 2011). In this paper, we report on a modified hydrothermal preparation yielding the  $\text{CoCr}_2\text{O}_4$  NPs with size ranging from 4.4 to 11.5 nm, which is comparable to the

characteristic size of the coherence of the spiral magnetic structure. The samples were characterized using different methods such as powder X-ray diffraction (PXRD), transmission electron microscopy (TEM), high-resolution TEM (HRTEM), scanning electron microscopy (SEM), thermogravimetric analysis (TGA), and Raman and infrared spectroscopy (FTIR). Basic characterization of the magnetic properties was also performed, and the results are discussed in the context of decreasing particle size.

## Experimental

### Sample preparation

The samples were prepared using the hydrothermal method. Following amounts of reactants were used for the preparation: 10 mmol (400 mg) of sodium hydroxide, 12 mmol (3.39 g) of oleic acid, and metal chlorides ( $\text{Cr}^{3+}:\text{Co}^{2+} = 2:1$ ). The preparation was carried out in the mixture of 15 ml of alcohol (ethanol/1-pentanol) and 20 ml of water. First, the sodium hydroxide was dissolved in a small amount of water, and then ethanol was added. This solution was mixed together with oleic acid to avoid the formation of soap (clear solution was formed instead). Then, the water solution of metal salts which served as a precursor was added, and the reaction mixture became sticky. Afterward, the solution was sonicated for 5 min. Two phases were formed: water and organic phase (Fig. 1), and the following reactions took part:

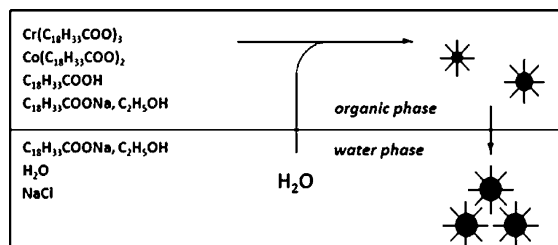
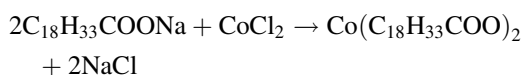
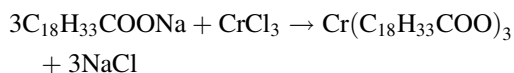


**Fig. 1** The process of formation of the  $\text{CoCr}_2\text{O}_4$  NPs. The metal salts are hydrolyzed and precipitated into the water phase after reaching a critical diameter

**Table 1** The preparation conditions for the NPs prepared by the hydrothermal procedure

Sample	Reaction composition				Reaction conditions		Annealing temperature (°C)
	Ratio Cr:Co (mmol)	Alcohol (ml)	Water (ml)	Oleic acid (ml)	Reaction temperature (°C)	Reaction time (h)	
DZ 300	2:1	Ethanol: 10	10	3.82	200	16	300
DZ 350	2:1	Ethanol: 20	20	3.82	200	16	350
DZ 400	2:1	1-Pentanol: 5	10	3.82	200	10	400
DZ 450	2:1	Ethanol: 10	15	6.37	200	16	450

This reaction mixture was put into a Teflon liner (volume 50 ml), enclosed in the autoclave, and placed into oven for 10–16 h at the reaction temperature of 200 °C. After cooling down the autoclave, the following phases were obtained: upper oleic phase, which contained a small amount of NPs, aqueous phase, and sedimented NPs. Liquid phase was discarded, and remaining NPs were dispersed in 15 ml of hexane. Then, the nondispersed NPs (aggregates) were separated using centrifugation, and hexane dispersion was used for the following preparation. Then, the NPs were precipitated from dispersion using 10 ml of ethanol and were separated by means of centrifugation (4,500 rpm for 5 min). This procedure (dissolving in hexane and precipitation using ethanol) was repeated for three times. The samples possessing amorphous phase were heat treated in the furnace at the final annealing temperatures. The preparation conditions for all samples are summarized in Table 1.

### Characterization methods

Powder X-ray diffraction was performed using the PANalytical X'Pert PRO diffractometer with Cu  $K_{\alpha}$  radiation ( $\lambda = 1.541874 \text{ \AA}$ ) equipped by secondary monochromator and PIXcel detector. All samples were measured in the  $2\theta$  range of 15–80° with the step of 0.02°. The particle diameter obtained from PXRD measurements was determined using two approaches: using the Scherrer's equation,  $d_{\text{Scherrer}} = k \cdot \lambda / (\beta \cdot \cos \theta)$  and by the Rietveld analysis,  $d_{\text{Rietveld}}$  implemented within the FullProf software (Rodríguez-Carvajal 2000). In both approaches, the instrumental broadening was considered.

Transmission electron microscopy was carried out using the JEOL 200CX device operating at 200 kV using two different modes: bright field (BF) and dark field (DF). The mean particle diameter,  $d_{\text{TEM}}$ , was

statistically determined from at least 100 particles for each sample using the log-normal distribution function.

High-resolution TEM images were captured with the JEM 2010 UHR device equipped with the Gatan imaging filter (GIF) and the 794 slow scan CCD. The samples for the TEM and HRTEM analysis were prepared by drying the dispersion of NPs on the coated copper grid.

Scanning electron microscopy images were obtained using the Tescan Mira I LMH device with the energy-dispersed X-ray detector (EDX) Bruker AXS. The powders were deposited on carbon film.

Thermogravimetric analysis was carried out using the STA 449 F1 Jupiter device. The samples were heated up to 600 °C (heating rate 10 °C/min) in argon atmosphere.

Raman spectra were measured using the Thermo Scientific DXR Raman Microscope with the Olympus microscope (objective 50×) in the spectral range of 50–1900  $\text{cm}^{-1}$  with the resolution of 3  $\text{cm}^{-1}$ . He–Ne laser or diode lasers (532 and 780 nm) were used for the measurement. The spectrometer was calibrated by calibration software using multiple neon emission lines and multiple polystyrene Raman bands and standardized by white light.

Raman and infrared spectroscopy spectra were obtained using the Thermo Scientific Nicolet 6700 FTIR spectrometer (resolution 2  $\text{cm}^{-1}$ , DTGS detector, KBr beam splitter, Happ-Ganzelapodization, KBr windows, and zero filling 2) in region 400–4000  $\text{cm}^{-1}$  with Nujol technique.

The zero-field-cooled (ZFC) and field-cooled (FC) magnetizations (applied field of 10 mT) and magnetization isotherms at selected temperatures were measured on the Quantum Design MPMS7XL device (SQUID). The temperature dependencies of the a.c. susceptibility were recorded in zero external magnetic

field at frequencies: 0.1, 1, 10,  $10^2$ , and  $10^3$  Hz with the amplitude of the a.c. magnetic field of 0.3 mT. The prepared samples were put into the capsule and fixed with the piece of polystyrene.

## Results and discussion

### Powder X-ray diffraction

Powder X-ray diffraction was used for determination of the phase composition, particles size, and lattice parameters of prepared samples. The measured diffraction patterns together with the refined profiles of the samples are shown in Fig. 2. All samples exhibit the characteristic diffractions corresponding to a cubic spinel phase with the space group  $Fd\bar{3}m$  (card No. JCPDF 22-1084). The small amount of NaCl has been detected in the DZ 350 and DZ 400 samples, probably due to nonsufficient washing procedure after the reaction, which has no negative impact on the physical properties of the spinel phase. Moreover, the DZ 350 sample contains also a small amount of  $Cr_2O_3$ .

The lattice parameter,  $a$  and NP diameters,  $d$  are summarized in Table 2. It has been observed that both the  $a$  and  $d$  increase with increasing annealing temperature. The  $a$  values of our samples are slightly lower than the tabulated ones ( $a = 8.3299$  Å, card No. JCPDF 22-1084). These effects can be explained by

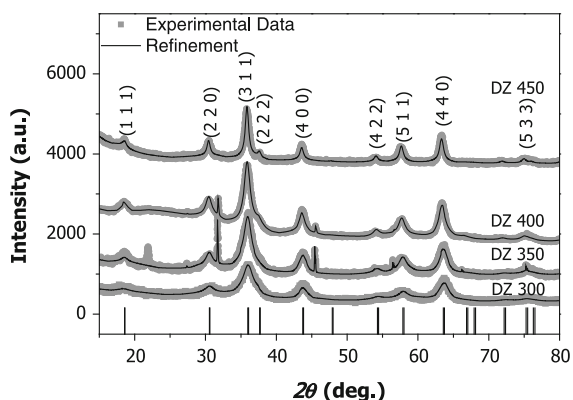


**Fig. 2** Experimental data of the PXRD measurements together with the fit using the Rietveld method. The vertical lines correspond to the positions of Bragg maxima of the  $CoCr_2O_4$  phase (card No. JCPDF 22-1084). The DZ 300 and DZ 450 samples are pure spinel phase. The DZ 400 sample also contains parasitic NaCl phase, and the DZ 350 sample exhibits presence of the NaCl and  $Cr_2O_3$  phases

defects present in crystal lattice (dislocation and vacancies) and by numerous dangling bonds on a NP surface, as is typical for small-sized NPs. The increase of  $a$  and  $d$  with the increasing annealing temperatures indicates the decrease of the structural disorder or cation redistribution within the spinel network (Sickafus et al. 1999). The particle diameters obtained from PXRD,  $d_{Scherrer}$ , and  $d_{Rietveld}$  are almost identical for all samples.

### Transmission electron microscopy

The BF mode images reveal spherical shape of the NPs. The DF mode provides additional information about crystallinity of the prepared NPs. The Figs. 3 and 4 show the TEM images of the samples together with the corresponding size distributions. It can be seen that the NPs are overlapping and have tendency to form aggregates with the increasing annealing temperature. Thus, the determination of  $d_{TEM}$  values for all samples serves only as a rough estimate of NP diameter and ranges from 6.7 to 11.5 nm for individual samples, respectively. Determined values correlate well with the  $d_{Rietveld}$  and  $d_{Scherrer}$  values in the range of the error (Table 2), which points at high crystallinity of the individual NPs.<sup>1</sup> The diffraction patterns of selected area measurements (SAED) were used for an additional determination of the phase composition of prepared samples (Fig. 5) and confirmed the presence of crystalline spinel cobalt chromite.

### High-resolution TEM

In addition, the DZ 300 sample was characterized using HRTEM, a typical image of the well-crystalline NPs and the corresponding SAED measurement are shown in Fig. 6. The results from SAED are also summarized in Table 3. The depicted value of the interplanar distances of 2.5 Å corresponds well with the (311) plane of the cobalt chromite spinel structure.

<sup>1</sup> Since the PXRD reflects the coherently diffracting volume of the particle and TEM size corresponds to the dimensions of the two-dimensional projection of the entire polycrystal in its specific orientation, the size obtained from PXRD should be almost identical to the TEM size in the case of the well-crystalline NP of approximately spherical shape.

**Table 2** Particle size determined from the TEM and PXRD. In the column PXRD, there are two values obtained by the simple estimation (Scherrer's equation),  $d_{\text{Scherrer}}$  and using the

Rietveld refinement,  $d_{\text{Rietveld}}$ . The  $d_{\text{TEM}}$  represents the values of median size of the particles revealed by the fit of the log-normal distribution. The  $a$  represents the lattice parameter

Sample	Annealing Temperature (°C)	PXRD		TEM	a (Å)
		$d_{\text{Scherrer}}$ (nm)	$d_{\text{Rietveld}}$ (nm)	$d_{\text{TEM}}$ (nm)	
DZ 300	300	4.9 ± 1.4	4.4 ± 0.5	6.7 ± 0.3	8.271(4)
DZ 350	350	5.4 ± 1.3	5.1 ± 0.5	5.9 ± 0.1	8.282(2)
DZ 400	400	6.9 ± 3.2	6.2 ± 0.5	6.4 ± 0.2	8.301(3)
DZ 450	450	11.8 ± 1.4	11.5 ± 0.1	11.5 ± 0.5	8.306(2)

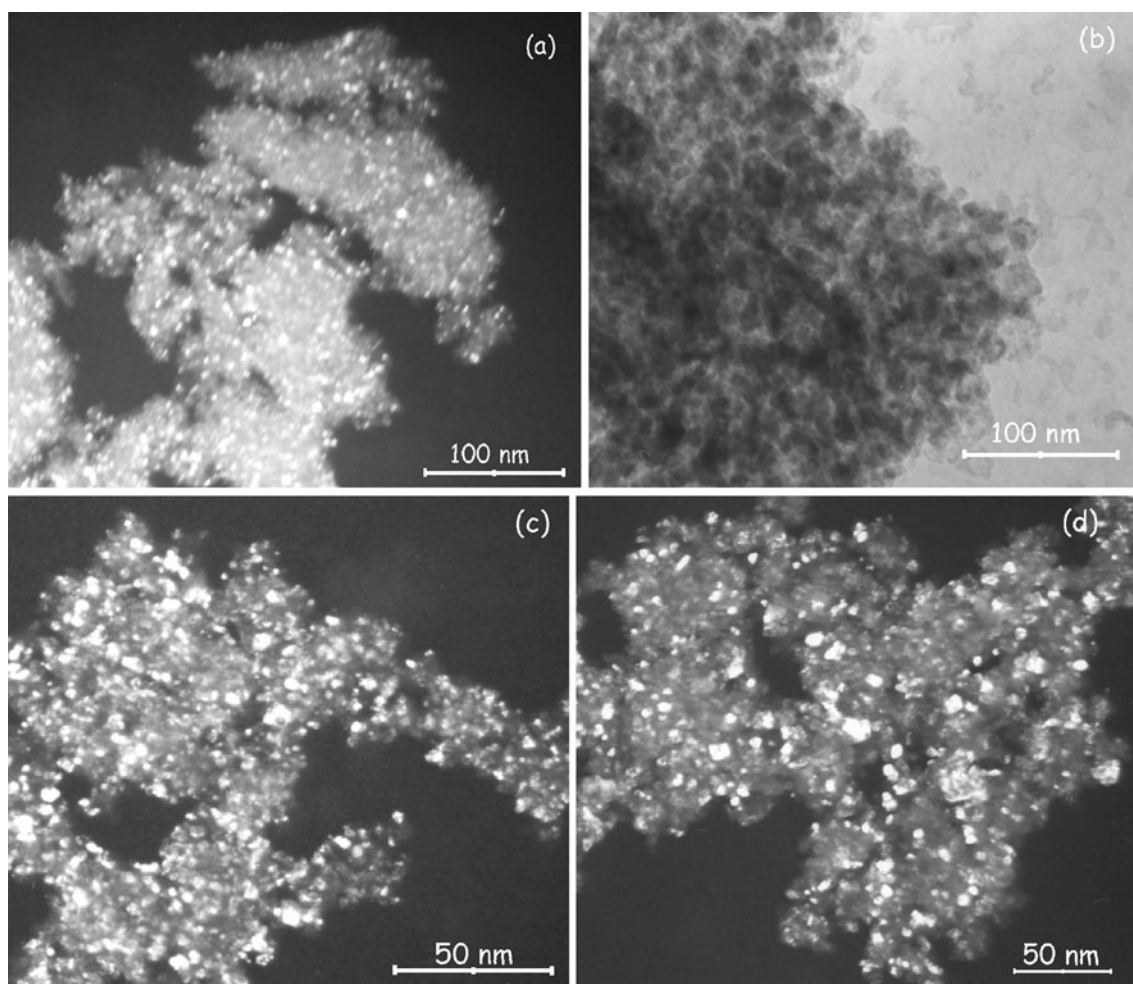


**Fig. 3** TEM images of the samples: **a** DZ 300 (DF mode), **b** DZ 350 (BF mode), **c** DZ 400 (DF mode), and **d** DZ 450 (DF mode)

#### EDX and TG analysis

The EDX analysis from SEM microscopy was used for the elemental analysis of the samples. The main

elemental components of the sample are Co, Cr, and O. The EDX analysis confirms that the atomic ratio between Co:Cr  $\cong$  1:2 (Co at. 18.19 %; Cr at. 36.79 %), as has been expected.

**Fig. 4** Histograms obtained from the BF mode of the TEM images. Size distribution was fitted using the log-normal distribution function with its maxima belonging to the median diameter of the particles,  $d_{TEM}$

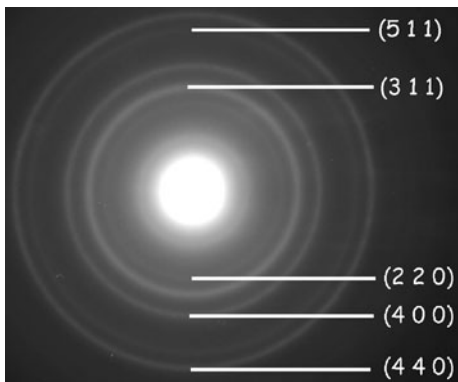
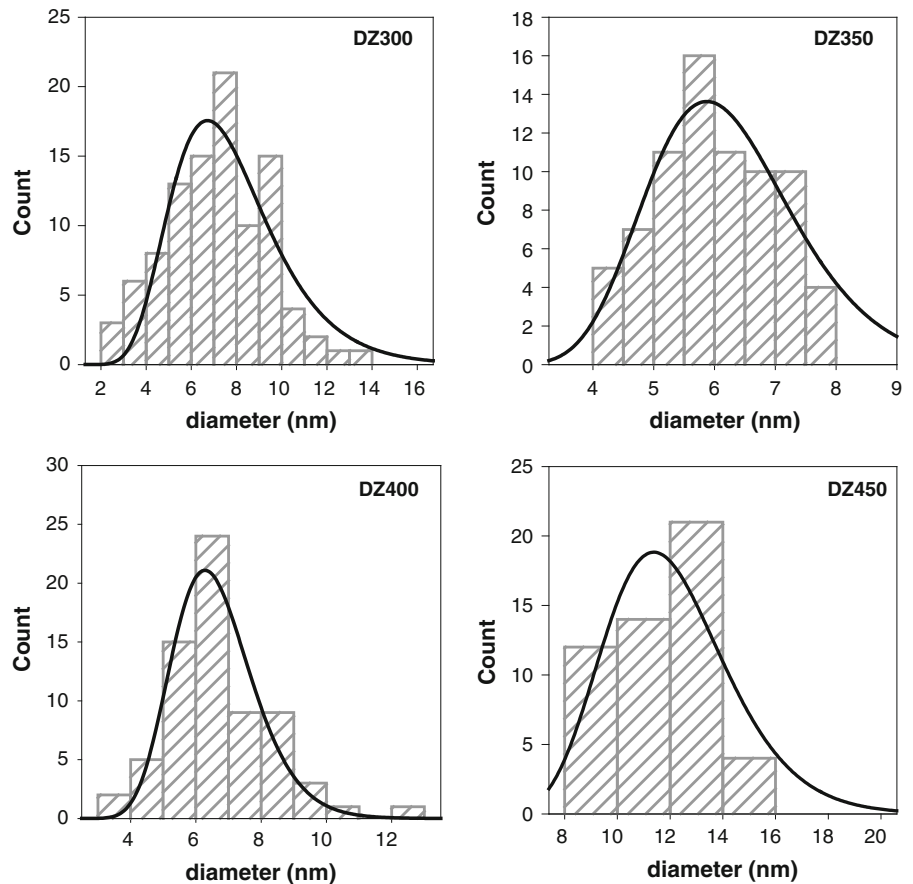


**Fig. 5** The SAED image of the DZ 300 sample. The solid lines mark the corresponding reflections of the spinel structure

Finally, the TG analysis was carried out to evaluate the organic and water content in the prepared samples. The results from the TG analysis of all prepared samples are shown in Fig. 7. The TG curves of the as-prepared samples show minimal weight losses up to

500 °C due to evaporation of absorbed water. The weight losses observed above 400 °C are attributed to organic remnants in the samples. The values of the amount of the organic content in the samples, determined from the total weight losses, are summarized in Table 4.

#### Vibrational spectroscopy

The  $\text{CoCr}_2\text{O}_4$  belongs to the normal cubic II-III spinels with the space group  $Fd\bar{3}m (O_h^7)$ . The atoms of  $\text{CoCr}_2\text{O}_4$  occupy the 8a ( $T_d$ ), 16d ( $O_h$ ), and 32e (oxygen) Wyckoff sites. These sites contribute to the  $F_{2g} + F_{1u}, A_{2u} + E_u + F_{2u} + 2F_{1u}$ , and  $A_{1g} + E_g + 2F_{2g} + F_{1g} + A_{2u} + E_u + F_{2u} + 2F_{1u}$  modes of theoretical vibrational representation. From these modes, the  $A_{1g}$ ,  $F_{2g}$  (triply degenerate), and  $E_g$  (doubly degenerate) are active in Raman spectra while four  $F_{1u}$  (triply degenerate) are IR active and one remaining  $F_{1u}$  is acoustic mode, and, therefore, cannot be

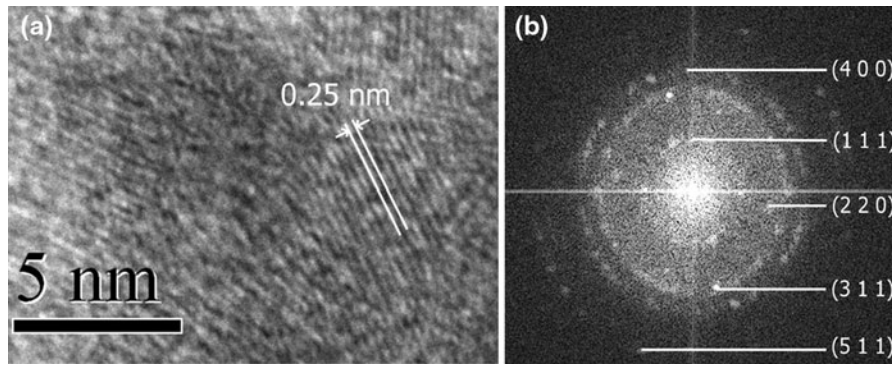


**Fig. 6** The HRTEM (a) and SAED b images of the DZ 300 sample

**Table 3** Assignments of the SAED image of the DZ 300 sample. The  $d_{hkl\_exp}$  corresponds to the experimental values, and  $d_{hkl\_st}$  corresponds to the standard values (card No. JCPDF 22-1084) of the interplanar distance values

hkl	(1 1 1)	(2 2 0)	(3 1 1)	(4 0 0)	(5 1 1)
$d_{hkl\_exp}$ (Å)	4.852	2.930	2.503	2.122	1.609
$d_{hkl\_st}$ (Å)	4.840	2.947	2.512	2.084	1.603

**Table 4** Results from TG analysis of the samples

Sample	Weight loss (mass %)	Organic content (mass %)
DZ 300	5.96	2.04
DZ 350	4.30	1.74
DZ 400	3.09	1.00
DZ 450	3.00	0.98

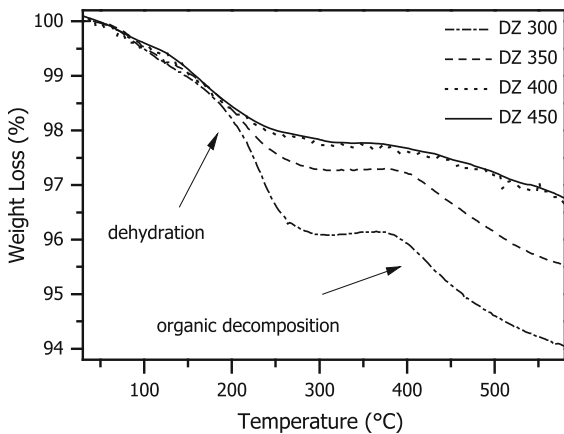


**Fig. 7** TG analysis of the samples

observed in the IR spectra. The rest of modes are both Raman ( $F_{1g}$ ) and IR ( $2A_{2u}$ ,  $2E_u$ , and  $2F_{2u}$ ) inactive modes. It was concluded from the theoretical prediction of the selection rules that Raman spectra of the pure cubic spinel consist of five fundamental bands ( $A_{1g} + E_g + 3F_{2g}$ ). These narrow bands are located at 686, 604, 515, 452, and 196  $cm^{-1}$  for the bulk  $CoCr_2O_4$  as was presented by Maczka et al. 2013. The narrow bands were also observed in nanosized

(20–25 nm)  $CoCr_2O_4$  in  $SiO_2$  matrix, but they were slightly shifted to 684  $cm^{-1}$  ( $A_{1g}$ ), 603  $cm^{-1}$  ( $F_{2g}(1)$ ), 514  $cm^{-1}$  ( $F_{2g}(2)$ ), 449  $cm^{-1}$  ( $E_g$ ), and 195  $cm^{-1}$  ( $F_{2g}(3)$ ); for the spectra see Fig. 8. The four  $F_{1u}$  bands active in the IR spectra were found at 630, 530, 380, and 190  $cm^{-1}$  in the bulk sample (Preudhomme and Tarte 1971a, b) and at 627  $cm^{-1}$  ( $F_{1u}(1)$ ), 532  $cm^{-1}$  ( $F_{1u}(2)$ ), 373  $cm^{-1}$  ( $F_{1u}(3)$ ), and 197  $cm^{-1}$  ( $F_{1u}(4)$ ) in nanosized  $CoCr_2O_4/SiO_2$ .

The Raman spectra of all samples contain five theoretically expected bands, but they are broader than those observed for bulk material (depicted in Fig. 9). Additional narrow (sharp) band located at 496  $cm^{-1}$  was observed in Raman spectra of the DZ 300 and DZ 350 samples. The position of the bands (predicted by theory) for mentioned samples and their interpretation are summarized in Table 5. The higher number of bands in the Raman spectra than was theoretically predicted can be explained using several ways. The presence of impurity phase can produce the additional Raman active band, however, all samples were found out to be nearly single phase, only the DZ 350 sample contained a small amount of  $Cr_2O_3$ , below the detection limit of Raman spectroscopy (band positions of  $Cr_2O_3$  are 616, 554, 529, 352, and 295  $cm^{-1}$ ). The

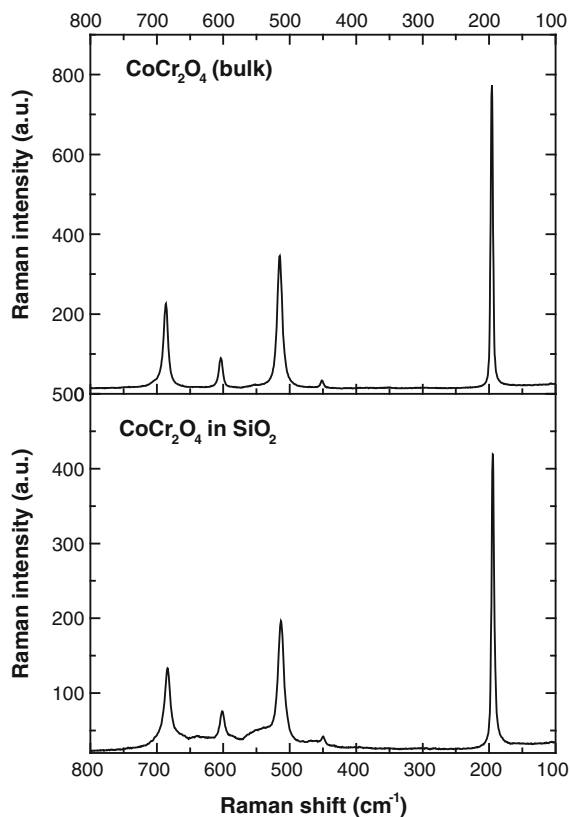


**Fig. 8** Raman spectra of the bulk (top panel) and NPs in the SiO<sub>2</sub> matrix (bottom panel) of the cobalt chromite NPs

one additional Raman band in the spectra cannot be also elucidated by the potential lowering of the cubic  $O_h$  symmetry to tetragonal  $D_{4h}$  symmetry caused by the Jahn–Teller effect. The observed lowering of symmetry to the tetragonal one is connected mainly with the bands of  $F_{1u}(1)$  and  $F_{1u}(2)$  in IR spectrum and  $F_{2g}(2)$  and  $F_{2g}(3)$  in Raman spectrum, as has been observed in the copper chromite (Khassin et al. 2009). However, this splitting is not observed in our spectra. The most probable origin of presence of one additional band in Raman spectra in the DZ 300 and DZ 350 samples can be the order–disorder effect (Da Rocha and Thibaudeau 2003; De Sousa Meneses et al. 2006; Laguna-Bercero et al. 2007; Maczka et al. 2013). The normal II–III, fully inverted, and partially inverted spinel structure belong to the same space group, and the same selection rules for vibrational spectra are applied. The fully (ideal) inverted spinel contains half of  $M^{III}$  ions in the  $T_d$ -sites and remaining half of  $M^{III}$  ions and all  $M^{II}$  ions in the  $O_h$ -sites. The described cation redistribution can lead to the shift of the Raman

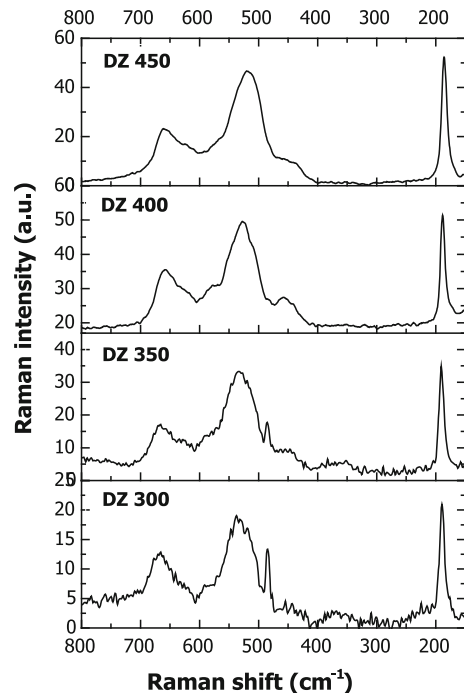


**Fig. 9** Raman spectra of the CoCr<sub>2</sub>O<sub>4</sub> samples

bands. The band assigned to the  $E_g$  symmetry is located at  $484\text{ cm}^{-1}$  in spectra of the DZ 300 and DZ 350 samples, while it is shifted to  $458$  and  $454\text{ cm}^{-1}$  in the spectra of the DZ 400 and DZ 450 samples, respectively. Both values of position of  $E_g$  symmetry bands predicted by theoretical calculation are located at  $485\text{ cm}^{-1}$  (Kushwaha and Kushwaha 2007) and  $454\text{ cm}^{-1}$  (Kushwaha 2009). The additional Raman active band at  $496\text{ cm}^{-1}$  can be attributed to the some degree of cation redistribution within the spinel network (Maczka et al. 2013). The change of intensity of additional Raman band can be influenced by the change of particle size. The decreasing particle size can lead to higher inverse spinel configuration in comparison with the bulk CoCr<sub>2</sub>O<sub>4</sub> that crystallizes predominantly in the normal spinel structure (Maczka et al. 2013).

The MID infrared spectrum with two broad more or less asymmetric bands with the centers approximately at  $620$  and  $520\text{ cm}^{-1}$  (Fig. 10), which are attributed to the  $\nu_1$  and  $\nu_2$  vibrations, was obtained (for the detailed assignment see Table 6). The broadness and asymmetry of these bands essentially depend on the nature of  $M^{III}$  cation and preparation conditions and do not depend on the nature and mass of the  $M^{II}$  cation

**Table 5** Interpretation of the CoCr<sub>2</sub>O<sub>4</sub> Raman spectra

Raman shift (cm <sup>-1</sup> )				Assignment	Symmetry
DZ 300	DZ 350	DZ 400	DZ 450		
190	190	190	186	$\delta$ (O–Co–O)	$F_{2g}(3)$
484	484	458	454	$\nu_s$ (Cr – O), $\nu_s$ (Co – O)	$E_g$
534	534	523	519	$\nu$ (Cr – O)	$F_{2g}(2)$
631	631	628	622	$\nu_s$ (Cr – O)	$F_{2g}(1)$
669	665	660	658	$\nu_s$ (Cr – O)	$A_{1g}$

(Preudhomme and Tarte 1971a, b, Sickafus et al. 1999). The bands can be assigned to the lattice of condensed octahedra. The  $\nu_3$  vibration seems to be related to the complex vibration involving the participation of both types of cations ( $T_d$  and  $O_h$ ). The last  $\nu_4$  vibration clearly depends on the mass of the M<sup>II</sup> cation and can be assigned to the vibration involving a displacement of the  $T_d$  cation. Some studies of isomorphic replacement of  $T_d$  and  $O_h$  cations were presented by Preudhomme and Tarte 1971a, b, Hosterman et al. 2013. It can be summarized that  $\nu_1$  and  $\nu_2$  vibrations are never split,  $\nu_3$  is split and shifted in the case of  $O_h$  cation replacement and only shifted in the case of  $T_d$  cation replacement, and  $\nu_4$  is split and shifted in the case of  $T_d$  cation replacement and no significant changes were observed in the case of  $O_h$  cation replacement. The very fine structure of these bands ( $\nu_1$  and  $\nu_2$ ) is not so sharp in the IR spectra of our samples, which is probably due to the nanosized dimension. The nanosized dimension of the samples leads to the broadness of the bands of the  $\nu_3$  and  $\nu_4$  vibrations in the FAR IR region. Therefore, it is not possible to make conclusions about the presence of partial  $T_d$  cation replacement observed in the IR spectra and it is not possible to confirm the effect observed in the Raman spectra of the DZ 300 and DZ 350 samples.

**Magnetic properties**

Magnetic behavior of the sample series was investigated by means of ZFC and FC magnetization recorded in moderate external magnetic field, magnetization isotherms at selected temperatures, and frequency-dependent a.c. magnetic susceptibility.

The temperature dependencies of the ZFC–FC magnetization are shown in Fig. 11. A furcation of the ZFC and FC curves (denoted as  $T_f$ ) followed by a

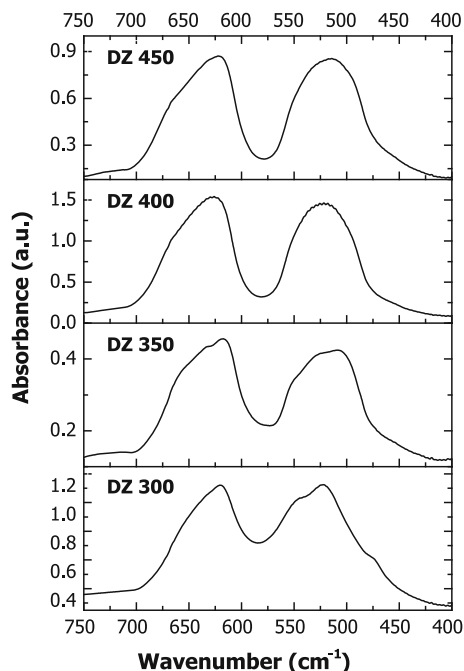


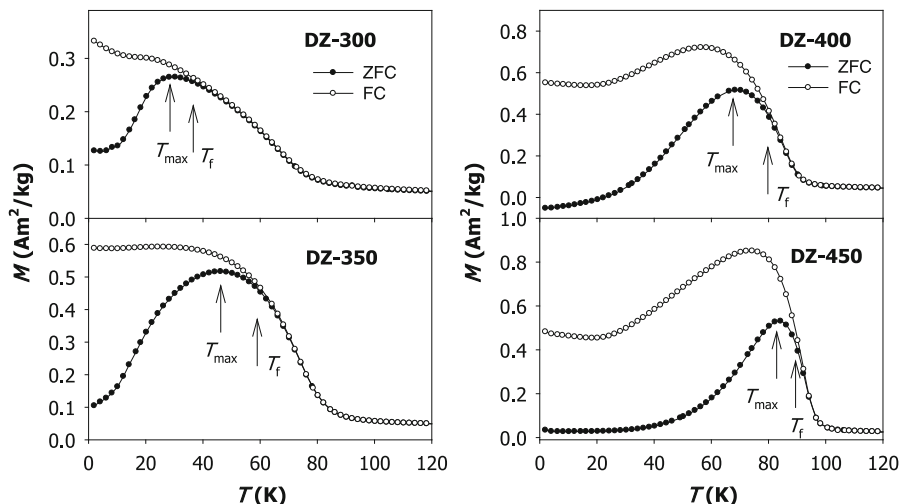
**Fig. 10** The Infrared spectra of the CoCr<sub>2</sub>O<sub>4</sub> samples using the laser with the wavelength of 532 nm

**Table 6** Interpretation of the CoCr<sub>2</sub>O<sub>4</sub> IR spectra

Wavenumber (cm <sup>-1</sup> )					
DZ	DZ	DZ	DZ	Assignment	Symmetry
300	350	400	450		
522	527	522	514	$\nu$ (Cr – O)	$F_{1u}(2)$
620	618	626	622	$\nu_{as}$ (Cr – O)	$F_{1u}(1)$

maximum on the ZFC curve on cooling ( $T_{max}$ ) can be observed in all samples; both the  $T_f$  and  $T_{max}$  shift to lower temperatures with decreasing particle size as depicted in Fig. 12. Figure 13 shows the temperature dependencies of the inverse ZFC and FC

**Fig. 11** Temperature dependencies of the zero-field-cooled (ZFC) and field-cooled (FC) magnetization,  $M$  of the DZ 300, DZ 350, DZ 400, and DZ 450 samples (measured at external magnetic field,  $\mu_0 H = 0.01$  T). The arrows mark the position of the ZFC–FC furcation ( $T_f$ ) and the maximum on the ZFC ( $T_{\max}$ )



magnetization that follow a typical functional form:  $\chi^{-1} = T/C + 1/\chi_0 - \sigma/(T - \theta_p)$ , consisting of a Curie–Weiss ferromagnetic term and a Curie paramagnetic term. Such behavior has been already reported for NPs of  $\text{MnCr}_2\text{O}_4$  and other ferrimagnetic spinels (Bhowmik 2006). The determination of the constants  $C$  and  $\sigma$  from this equation is problematic, because they are coupled in the paramagnetic regime; however, an estimation of the so-called asymptotic Curie temperature,  $\theta_p^a$ , can be obtained by extrapolation of the  $1/M$  data in the vicinity of the  $T_f$ , as shown in Fig. 13. The closer to the bulk ordering temperature,  $T_c$ , the better developed long-range ferrimagnetic order; in other words, the increasing magnetic disorder in NPs is manifested by the large difference between the  $\theta_p^a$  and  $T_c$ . According to the core–shell model of ferrimagnetic NPs (Kodama et al. 1996), the disorder is usually associated with the increasing contribution of shell surface spins while the long-range ferrimagnetic order is related to core spins. In our samples, the  $\theta_p^a$  shifts to significantly lower values with decreasing particle size, as shown in Fig. 12, suggesting substantial of spin disorder.

The first order derivatives of the ZFC and FC curves are presented in Fig. 14. The minimum for the ZFC becomes broad and less pronounced for NPs with decreasing size, which is related to the above-mentioned disorder effects in NP samples. This is implied by the fact that the sample is magnetically more ordered in the FC state than the ZFC state. The first-order derivative does not show additional sharp extremes, indicating that the noncollinear spin

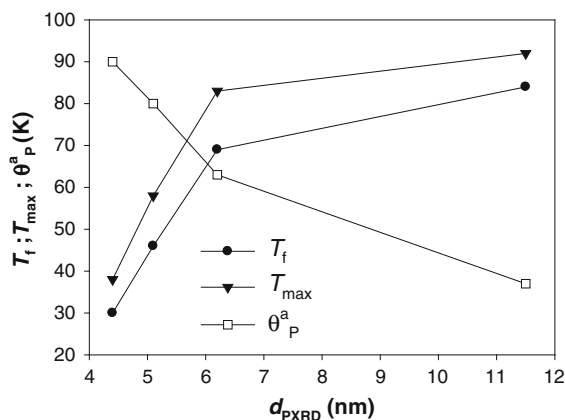


**Fig. 12** The dependence of the furcation temperature,  $T_f$ ; temperature of the ZFC maxima,  $T_{\max}$ ; and the Curie temperature,  $\theta_p^a$ , on the particle diameter determined using PXRD,  $d_{\text{PXRD}}$

configuration below the  $T_s$  and  $T_{\text{lock-in}}$  lacks or weakens in the NPs. The difference between the ZFC and FC magnetizations, shown in Fig. 14, corroborates the gradual increase of the spin disorder with decreasing particle size. Except the  $T_f$ -related anomaly and a single inflex point at about 30–60 K present in all samples, the DZ 450 sample shows a shallow minimum around 20 K suggesting presence of the bulk-like order-to-order magnetic phase transitions. Shift of the ZFC minimum of NP samples to higher temperature indicates the increase of the ordering temperature with the increasing particle size, which is a trend opposite to that observed for the  $\text{MnCr}_2\text{O}_4$  NPs (Bhowmik 2006), but corresponds to

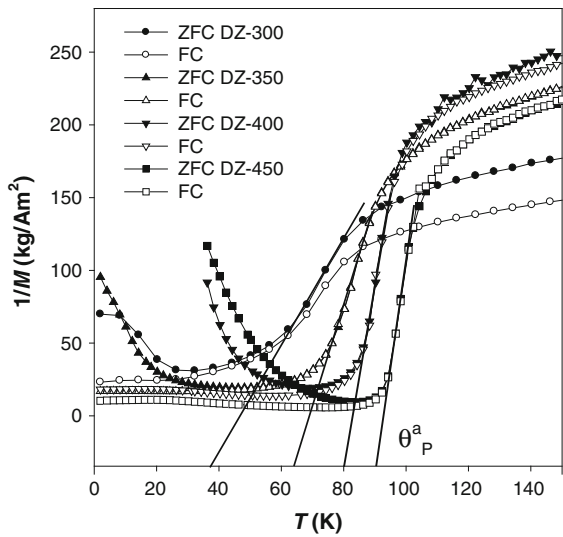


**Fig. 13** Temperature dependencies of the inverse zero-field-cooled (ZFC) and field-cooled (FC) magnetization together with the asymptote of the paramagnetic Curie temperature,  $\theta_p^a$

the evolution of the spin disorder with the particle size. As reported previously (Dutta et al. 2009; Rath et al. 2011), the particles with size about 40 nm exhibit magnetic properties very similar to the bulk  $\text{CoCr}_2\text{O}_4$  compound with the ordering temperature of about 85 K represented by a dominant maximum on the ZFC magnetization. Additional magnetic phase transitions related to the  $T_s$  and also  $T_{\text{lock-in}}$  temperatures can be observed either on the a.c. susceptibility (Dutta et al. 2009) or specific heat (Rath et al. 2011). Nevertheless, the considerable size distribution of the NPs reported in (Dutta et al. 2009, Rath et al. 2011) causes minor variations in the  $T_s$  and  $T_{\text{lock-in}}$  resulting in less-pronounced anomalies in contrast to sharp peaks observed on single crystals or polycrystalline samples of  $\text{CoCr}_2\text{O}_4$ . On the other hand, the particles in our study exhibit a relatively narrow size distribution and the size converges to the typical correlation length of the spiral component in the ground state of the magnetic structure [ $\sim 3.1$  nm (Tomiyasu et al. 2004)]. Hence, a significant suppression of the long-range magnetic order, at least at the ground state magnetic phase, is expected.

The typical magnetization isotherms of the samples with the border particle sizes (DZ 300 and DZ 450) are shown in Figs. 15 and 16. The magnetization curves carried out above the  $T_f$  show linear dependence on the applied field without hysteresis as is generally

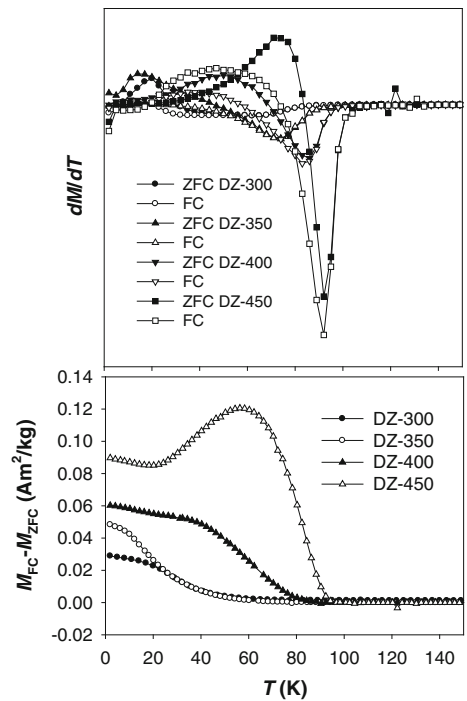


**Fig. 14** Temperature dependencies of the first derivative of the zero-field-cooled (ZFC) and field-cooled (FC) magnetization (top panel) and difference of the ZFC and FC magnetizations (bottom panel) (measured at external magnetic field,  $\mu_0 H = 0.01$  T)

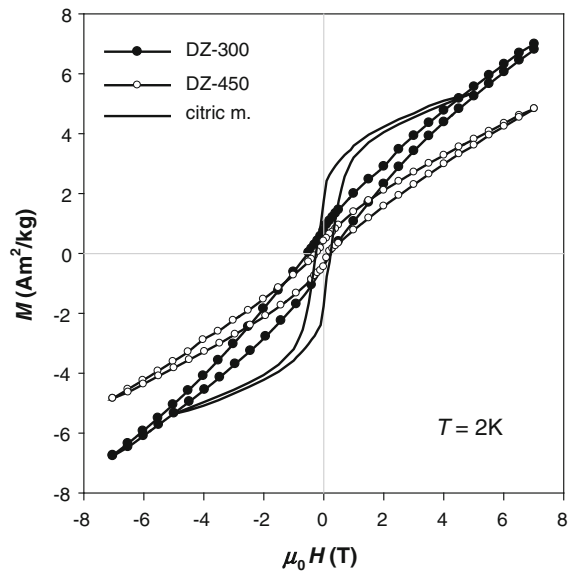


**Fig. 15** Typical magnetization isotherms ( $T = 2$  K) of the samples annealed at the lowest (DZ 300) and the highest (DZ 450) temperature in comparison to the bulk sample prepared using the citric method (citric m.)

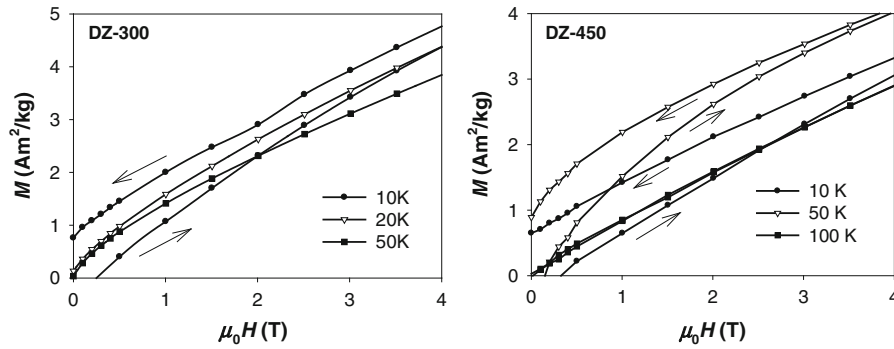


**Fig. 16** Details of the magnetization isotherms of the DZ 300 and DZ 450 samples. For the DZ 300 sample, the curves are measured at selected temperatures below the  $T_f$ . For the DZ 450 sample, the curves are recorded at the temperatures corresponding to the

ground state (10 K), ferrimagnetic (50 K), and paramagnetic (100 K) phase in the bulk  $\text{CoCr}_2\text{O}_4$ . The arrows indicate branches of the curves with hysteresis corresponding to the increasing/decreasing applied magnetic field

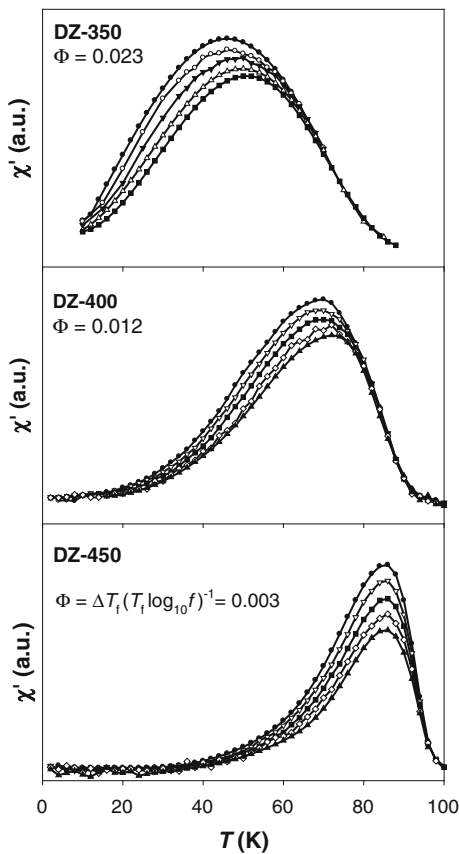


**Fig. 17** Temperature dependence of the real part of the a.c. magnetic susceptibility,  $\chi'$  recorded in the frequencies: 0.1, 1, 10,  $10^2$ , and  $10^3$  Hz; the maxima exhibit a moderate shift to higher temperatures with the increasing frequency

characteristic for paramagnetic phases. Those measured at 2 K show moderate hysteresis of  $\sim 0.2$  T, which is about two orders larger than that reported for a single crystal (Tomiyasu et al. 2004), but comparable to the coercivity,  $H_c$ , of the polycrystalline sample (shown for comparison in Fig. 15). The enhancement of the  $H_c$  can be usually observed in nonstoichiometric samples or in samples containing a small amount of antiferromagnetic phases like  $\text{CoO}$  or  $\text{Cr}_2\text{O}_3$  (not detectable by PXRD) in contact with the NPs, which can be involved in the exchange-bias phenomena (EB). Inspecting carefully both the positive and negative values of the  $H_c$  after FC (not shown), a clear shift of the hysteresis loop to the negative fields occurs, which supports the role of the EB in the  $H_c$  enhancement. The values of the EB field [defined as:  $H_{\text{EB}} = (H_c^+ - H_c^-)/2$ ] are 0.140, 0.055, and 0.025 T for the DZ 450, DZ 300, and reference samples, respectively. Nevertheless, the magnetization does not saturate even in the field of 7 T suggesting that the fraction of the ordered sample is rather low and thus the EB is a matter of a minor sample volume. The overall lack of saturation can be attributed either to the surface spin disorder (Kodama et al. 1997), or it can be rather explained by the formation of the glassy-like state. With increasing temperature to the  $T_f$ , the magnetization isotherms of the DZ 300 sample show monotonous decrease of both the  $H_c$  and remanence, while those of the DZ 450 sample exhibit a sudden increase of the remanence at about 50 K suggesting

transition to a different magnetic phase as observed in the bulk sample.

The temperature dependencies of the real part of the a.c. susceptibility of the DZ 350, DZ 400, and DZ 450 samples are shown in Fig. 17. The curves show a single maxima for each frequency ( $f$ ), which shift to higher temperatures with increasing  $f$ , as expected. In order to classify the nature of the relaxation processes in the samples, a simple estimation of the relative shift of the maximum temperature per frequency decade was performed (Goya et al. 2003). The corresponding parameter,  $\Phi$ , is defined as  $\Delta T^*(T^*\log_{10}f)^{-1}$ , where  $T^*$  is the temperature of the susceptibility maximum at given frequency,  $f$ . The  $\Phi$  values decrease with the increasing particle size as 0.023, 0.012, and 0.003 for the DZ 350, DZ 400, and DZ 450 samples, respectively. Typically, the  $\Phi$  values about 0.02–0.05 suggest formation of concentrated spin-glass (SG) or cluster-glass (CG) states, usually in the surface layer (shell) of the NPs (Dormann et al. 1997; Li et al. 2003); the  $\Phi$  values in order of 0.001 are either characteristic for canonical SG or ferromagnetic CG compounds (Nishioka et al. 2000) or suggest formation of rather well-ordered magnetic phase. Considering the previously discussed results of the magnetization measurements, the a.c. susceptibility study corroborates the proposed increase of the spin disorder in NPs with decreasing particle size, leading to suppression of the long-range ferrimagnetic order.

## Conclusions

The hydrothermal method in oleic acid–sodium oleate–water–ethanol was successfully used for the preparation of well-crystalline cobalt chromite NPs with the size ranging from 4.4 to 11.5 nm, yielding the as-prepared NPs capped by the oleic acid. The mechanism of the NP formation in the oleic acid–sodium oleate–water system was also proposed. The water and organic content was determined using the TGA; the as-prepared particles contain about 2 % of the organic phase. It was found that the particles size increases with the increasing annealing temperature, as expected, and the size distribution, determined from the TEM analysis, is relatively narrow. The Raman and FTIR spectroscopy studies confirmed presence of inverse spinel structure; however, additional bands related to disorder were also observed.

Finally, magnetic properties of the samples were investigated and related to the particle size. Typical features of glassy-like state become more pronounced with the decreasing particle size, as it is evidenced by the temperature and in-field dependence of magnetization and frequency-dependent a.c. susceptibility. The shift of the ZFC–FC furcation point ( $T_f$ ) and the maxima on the ZFC curve ( $T_{\max}$ ) toward lower temperatures with the decreasing particle size are attributed to continuous increase of the spin disorder. While the ferrimagnetic order still dominates in the largest particles, it almost collapses in the sample with the least particle size close to the coherence length of the spin wave in the ground state magnetic structure. As the magneto-electric coupling in the bulk  $\text{CoCr}_2\text{O}_4$  is believed to be conditioned by formation of the spiral magnetic phase, a study of dielectric properties with respect to the particle size is of high demand to clear up the scenario of multiferroicity in the  $\text{CoCr}_2\text{O}_4$  and related compounds.

**Acknowledgment** This study was supported by the Grant Agency of the Czech Republic under Project No. P108/10/1250 and by the Long-Term Research Plan of the Ministry of Education of the Czech Republic (MSM0021620857). Magnetic measurements were performed in MLTL (see: <http://mltl.eu>), which is supported within the program of Czech Research Infrastructures (Project No. LM2011025).

## References

- Bhowmik RN (2006) Lattice expansion and noncollinear to collinear ferrimagnetic order in a  $\text{MnCr}_2\text{O}_4$  nanoparticle. *Phys Rev B* 73:144413. doi:10.1103/PhysRevB.73.144413
- Chang LJ, Huang DJ, Li W-H et al (2009) Crossover from incommensurate to commensurate magnetic orderings in  $\text{CoCr}_2\text{O}_4$ . *J Phys Condens Matter* 21(45):456008. doi:10.1088/0953-8984/21/45/456008
- Da Rocha S, Thibaudeau P (2003) Ab initio high-pressure thermodynamics of cationic disordered  $\text{MgAl}_2\text{O}_4$  spinel. *J Phys Condens Matter* 15:7103–7115. doi:10.1088/0953-8984/15/41/018
- De Sousa Meneses D, Brun JF, Rousseau B, Echegut P (2006) Polar lattice dynamics of the  $\text{MgAl}_2\text{O}_4$  spinel up to the liquid state. *J Phys Condens Matter* 18:5669–5686. doi:10.1088/0953-8984/18/24/008
- Dormann JL, Fiorani D, Tronc E (1997) Magnetic relaxation on fine-particle systems. *Adv Chem Phys* 98:326
- Durrani SK, Hussain SZ, Saeed K (2012) Hydrothermal synthesis and characterization of nanosized transition metal chromite spinels. *Turk J Chem* 36:111–120. doi:10.3906/kim-1104-61
- Dutta DP, Manjanna J, Tyagi AK (2009) Magnetic properties of sonochemically synthesized  $\text{CoCr}_2\text{O}_4$  nanoparticles. *J Appl Phys* 106(4):043915. doi:10.1063/1.3204659

- Edrissi M, Keshavarz AR (2012) Synthesis of cobalt chromite nanoparticles by thermolysis of mixed  $\text{Cr}^{3+}$  and  $\text{Co}^{2+}$  chelates of 2-mercaptopyridin *N*-oxide. *Nano Micro Lett* 4(2):83–89. doi:[10.3786/nml.v4i2.p83-89](https://doi.org/10.3786/nml.v4i2.p83-89)
- Funahashi S, Morii Y, Child HR (1987) Two dimensional neutron diffraction of  $\text{YFe}_2\text{O}_4$  and  $\text{CoCr}_2\text{O}_4$ . *J Appl Phys* 61:4114. doi:[10.1063/1.338520](https://doi.org/10.1063/1.338520)
- Goya GF, Berquo TS, Fonseca FC, Morales MP (2003) Static and dynamic magnetic properties of spherical magnetite nanoparticles. *J Appl Phys* 94:3520
- Hastings JM, Corliss LM (1962) Magnetic structure of manganese chromite. *Phys Rev* 126:556–565. doi:[10.1103/PhysRev.126.556](https://doi.org/10.1103/PhysRev.126.556)
- Hosterman BD, Farley JW, Johnson AL (2013) Spectroscopic study of the vibrational modes of magnesium nickel chromite,  $\text{Mg}_x\text{Ni}_{1-x}\text{Cr}_2\text{O}_4$ . *J Phys Chem Solids* 74:985–990. doi:[10.1016/j.jpccs.2013.02.017](https://doi.org/10.1016/j.jpccs.2013.02.017)
- Khassin AA, Kustova GN, Jobic H, Yurieva TM, Chesalov YA, Filonenko GA, Plyasova LM, Parmon VN (2009) The state of absorbed hydrogen in the structure of reduced copper chromite from the vibration spectra. *Phys Chem Chem Phys* 11:6090–6097. doi:[10.1039/b821381j](https://doi.org/10.1039/b821381j)
- Kim I, Oh YS, Liu Y et al (2009) Electric polarization enhancement in multiferroic  $\text{CoCr}_2\text{O}_4$  crystals with Cr-site mixing. *Appl Phys Lett* 94(4):042505. doi:[10.1063/1.3076102](https://doi.org/10.1063/1.3076102)
- Kodama RH, Berkowitz AE, McNiff EJ, Foner S (1996) Surface spin disorder in  $\text{NiFe}_2\text{O}_4$  nanoparticles. *Phys Rev Lett* 77(2):394. doi:[10.1103/PhysRevLett.77.394](https://doi.org/10.1103/PhysRevLett.77.394)
- Kodama RH, Berkowitz AE, McNiff EJ, Foner S (1997) Surface spin disorder in ferrite nanoparticles. *J Appl Phys* 81(8):5552. doi:[10.1063/1.364659](https://doi.org/10.1063/1.364659)
- Kushwaha AK (2009) Study of interatomic interactions in chromite spinel  $\text{CoCr}_2\text{O}_4$ . *Chin J Phys* 47(3):355–360
- Kushwaha AK, Kushwaha SS (2007) Zone-centre phonon frequencies of oxide spinels. *Chin J Phys* 45(3):363–373. doi:[org/10.1016/j.physb.2008.05.022](https://doi.org/10.1016/j.physb.2008.05.022)
- Laguna-Bercero MA, Sanjuan ML, Merino RI (2007) Raman spectroscopic study of cation disorder in poly- and single crystals of the nickel aluminate spinel. *J Phys Condens Matter* 19:186217. doi:[10.1088/0953-8984/19/18/186217](https://doi.org/10.1088/0953-8984/19/18/186217)
- Li DX, Nimori S, Shiokawa Y, Haga Y, Yamamoto E, Onuki Y (2003) Ferromagnetic clusters glass behaviour in  $\text{U}_2\text{IrSi}_3$ . *Phys Rev B* 68:172405. doi:[10.1103/PhysRevB.68.172405](https://doi.org/10.1103/PhysRevB.68.172405)
- Lyons DH, Kaplan TA, Dwight K, Menyuk N (1962) Erratum: classical theory of the ground spin-state in cubic spinels. *Phys Rev* 126:540. doi:[10.1103/PhysRevB.72.099902](https://doi.org/10.1103/PhysRevB.72.099902)
- Maczka M, Ptak M, Kurnatowska M, Hanuza J (2013) Synthesis, phonon and optical properties of nanosized  $\text{CoCr}_2\text{O}_4$ . *Mater Chem Phys* 138(2–3):682–688. doi:[10.1016/j.matchemphys.2012.12.039](https://doi.org/10.1016/j.matchemphys.2012.12.039)
- Menyuk N, Dwight K, Wold A (1964) Ferrimagnetic spiral configurations in cobalt chromite. *J Phys* 25:528–536. doi:[10.1051/jphys:01964002505052801](https://doi.org/10.1051/jphys:01964002505052801)
- Nishioka T, Tabata Y, Taniguchi T, Miyako Y (2000) Canonical spin glass behaviour in  $\text{Ce}_2\text{AgIn}_3$ . *J Phys Soc Jpn* 69:1012. doi:[10.1143/JPSJ.69.1012](https://doi.org/10.1143/JPSJ.69.1012)
- Preudhomme J, Tarte P (1971a) Infrared studies of spinels—I: a critical discussion of the actual interpretations. *Spectrochim Acta Part A* 27(7):961–968. doi:[10.1016/0584-8539\(71\)80179-4](https://doi.org/10.1016/0584-8539(71)80179-4)
- Preudhomme J, Tarte P (1971b) Infrared studies of spinels—III: the normal II–III spinels. *Spectrochim Acta Part A* 27(9):1817–1835. doi:[10.1016/0584-8539\(71\)80235-0](https://doi.org/10.1016/0584-8539(71)80235-0)
- Rath C, Mohanty P (2010) Magnetic phase transitions in cobalt chromite nanoparticles. *J Supercond Nov Magn* 24(1–2):629–633. doi:[10.1007/s10948-010-0958-7](https://doi.org/10.1007/s10948-010-0958-7)
- Rath C, Mohanty P, Banerjee A (2011) Magnetic properties of nanoparticles of cobalt chromite. *J Magn Magn Mater* 323(12):1698–1702. doi:[10.1016/j.jmmm.2011.01.040](https://doi.org/10.1016/j.jmmm.2011.01.040)
- Repko A, Nižňanský D, Poltiová-Vejpravová J (2011) A study of oleic acid-based hydrothermal preparation of  $\text{CoFe}_2\text{O}_4$  nanoparticles. *J Nanopart Res* 13:5021–5031. doi:[10.1007/s11051-011-0483-z](https://doi.org/10.1007/s11051-011-0483-z)
- Rodríguez-Carvajal J (2000) FullProf User's guide manual. CEA-CRNS, France
- Shirane G, Cox DE, Pickart SJ (1964) Magnetic structures in  $\text{FeCr}_2\text{S}_4$  and  $\text{FeCr}_2\text{O}_4$ . *J Appl Phys* 35:954–955. doi:[10.1088/1367-2630/10/5/055014](https://doi.org/10.1088/1367-2630/10/5/055014)
- Sickafus KE, Wills JM, Grimes NW (1999) Structure of spinel. *J Am Ceram Soc* 82(12):3279–3292. doi:[10.1111/j.1151-2916.1999.tb02241.x](https://doi.org/10.1111/j.1151-2916.1999.tb02241.x)
- Tomiyasu K, Fukunaga J, Suzuki H (2004) Magnetic short-range order and reentrant-spin-glass-like behavior in  $\text{CoCr}_2\text{O}_4$  and  $\text{MnCr}_2\text{O}_4$  by means of neutron scattering and magnetization measurements. *Phys Rev B* 70(21):214434. doi:[10.1103/PhysRevB.70.214434](https://doi.org/10.1103/PhysRevB.70.214434)
- Yamasaki Y, Miyasaka S, Kaneko Y et al (2006) Magnetic reversal of the ferroelectric polarization in a multiferroic spinel oxide. *Phys Rev Lett* 96(20):207204. doi:[10.1103/PhysRevLett.96.207204](https://doi.org/10.1103/PhysRevLett.96.207204)